PERMAFROST AND PERIGLACIAL PROCESSES
Permafrost and Periglac. Process. **16**: 277–290 (2005)
Published online in Wiley InterScience (www.interscience.wiley.com). DOI: 10.1002/ppp.531

Quantifying Permafrost Patterns using Minkowski Densities

Kurt Roth,[1]* *Julia Boike*[2] *and Hans-Jörg Vogel*[1]

[1] Institute of Environmental Physics, University of Heidelberg, Heidelberg, Germany
[2] Alfred-Wegener-Institute for Polar and Marine Research, Potsdam, Germany

ABSTRACT

Minkowski densities and density functions are measures for quantifying arbitrary binary patterns. They are employed here to describe permafrost patterns obtained from aerial photographs. We demonstrate that images taken at two neighbouring sites shown distinctly different patterns and quantify the difference. It is found that one of the sites exhibits an essentially single-scale structure while the other one has a multiscale organization. Minkowski densities and density functions are thus proposed as sensitive and objective measures to quantify the change of permafrost patterns in space or in time. Copyright © 2005 John Wiley & Sons, Ltd.

KEY WORDS: permafrost; patterned ground; density functions

INTRODUCTION

Permafrost forms like sorted circles, hummocks, polygons, and stripes are spectacular manifestations of the complex dynamics of periodically frozen soils. Their structure depends on the parent material as well as on the external forcing by the thermal and hydraulic regime (Hallet, 1990) and by possible fluxes of solid matter (Francou *et al.*, 2001). While these forms are interesting in their own right as examples of self-organized natural systems (Kessler *et al.*, 2001), they may be even more interesting as indicators of changing environmental conditions which would lead to changing patterns. These can be observed rather inexpensively and over large regions through aerial photographs. A major hurdle in this approach is the objective quantification of observed patterns. While easily recognized and categorized by eye, they are notoriously difficult to cast into numbers which is a prerequisite for quantifying changes. A popular approach to this problem is to interpret the pattern as a realization of some random space function and to estimate its statistical properties, in particular covariance functions of various order and correlation lengths (Journel and Huijbregts, 1978; van Kampen, 1981). A difficulty with this approach is that already moderately complicated patterns require higher order covariance functions which are hard to estimate for natural patterns that in general are not stationary. Alternatively, the pattern may be interpreted as a fractal object whose dimension and generator are to be determined (Mandelbrot, 1977; Bacry *et al.*, 2001). Difficulties here are that there is hardly ever a single underlying generator and that the available data do not cover sufficiently many scales. While both approaches have been demonstrated for describing various patterns they appear less attractive for quantifying patterns in permafrost soils. In this paper, we follow a different approach, interpret the patterns as arbitrary geometric objects and use Minkowski numbers and functions (Mecke, 2000) to characterize them.

THEORY

Minkowski Numbers

A quantitative geometric description aims to reduce the complexity of an object to a limited number of

* Correspondence to: Kurt Roth, Institute of Environmental Physics, INF 229, University of Heidelberg, D-69120 Heidelberg, Germany. E-mail: kurt.roth@iup.uni-heidelberg.de

Received 27 October 2003
Revised 23 March 2005
Accepted 14 April 2005

relevant quantities. In our context, relevant means that the chosen measures distinguish between characteristic patterns. Such measures should satisfy some basic requirements so that the results obtained for different patterns and by different observers are comparable. Specifically, these requirements are:

Additivity: The results obtained for the unification of two subregions X and Y should be the same as the summation of the results obtained for the individual subregions, properly accounting for their overlap which has been counted twice. For the measure M this may be formulated as $M(X \cup Y) = M(X) + M(Y) - M(X \cap Y)$. Additivity is especially important, since we are typically not in the position to study a given pattern as a whole but are analysing limited regions.

Motion invariance: The results must not change if a given object is moved or rotated, hence are independent of the position of the observer.

Continuity: Small changes of a given object must lead to small changes of the measure. Since imaging techniques are typically afflicted with various types of noise, the measure should be robust in this context.

In the following we assume that the object of interest is the set X of black pixels of some binary structure Ω, hence $X \subset \Omega$. Specifically, the object X might represent stones, vegetation or bare soil and Ω is the image to be analysed. Given such a binary image, integral geometry provides $d+1$ basic measures, where d is the dimension of Ω. These measures are called 'Minkowski numbers' M_k and satisfy the requirements mentioned above. The first measure M_0 is simply the mass of the structural unit, which in two dimensions is its surface area A. Hence

$$M_0(X) = A(X) \tag{1}$$

The other Minkowski numbers are defined through integrals over the boundary ∂X of the object X. Notice that ∂X defines the shape of X unambiguously. In d-dimensional space there are d basic integrals related to the boundary and its $d-1$ principle radii of curvature. For $d = 2$ the first integral measures the total length of the boundary,

$$M_1(X) = \int_{\partial X} \mathrm{d}s = L(X) \tag{2}$$

and the second integral measures the total curvature of the boundary,

$$M_2(X) = \int_{\partial X} \frac{1}{r} \mathrm{d}s = C(X) \tag{3}$$

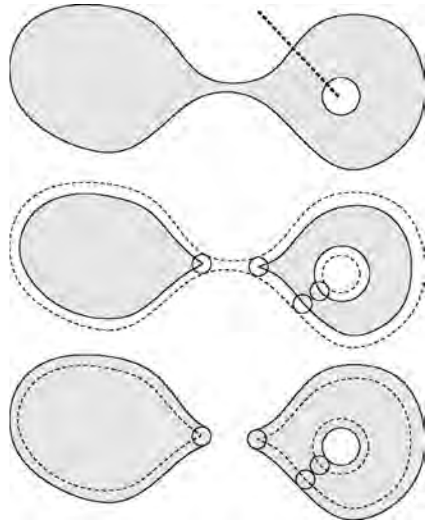

Figure 1 Sketch for Euler number defined in (4) and its change upon opening. The topmost pattern consists of one single object with one redundant connection: cutting along the dashed line removes one connection without generating a new object. Any (topologically) different cut creates a new object, the corresponding connection is thus not redundant. Hence, with (4), $\chi = 0$. The first step to opening this pattern consists of eroding it with a circular element of radius r. This leads to the grey pattern in the middle. The second step consists of dilating, adding a 'skin' of thickness r and produces the pattern at the bottom. Opening with radius r removes all smaller features, here the narrow ridge between the larger patches. For the opened pattern, $\chi = 1$.

where ds is the boundary element and r is its radius of curvature, positive for convex and negative for concave shapes. Notice that the curvature integral equals 2π for each closed convex boundary (objects) and -2π for each closed concave boundary (holes). Thus, M_2 is closely related to the Euler number χ which counts the number N_{object} of isolated objects minus the number N_{hole} of holes within the objects, which are also referred to as loops (see top of Figure 1). In particular

$$\chi(X) = N_{\text{object}} - N_{\text{hole}} = \frac{1}{2\pi} M_2(X) \tag{4}$$

M_2 is a dimensionless topological measure that quantifies the connectivity of the pattern while M_1 and M_0 are metric entities with units [L] and [L^2], respectively.

To compare results obtained from different images, we remove the effect of image size through normalization with respect to the total area A(Ω) of the region considered. Thus, we introduce the Minkowski densities

$$m_k(X) := \frac{M_k(X \cup \Omega)}{A(\Omega)} \tag{5}$$

as intensive quantities and will use them throughout this paper.

Hadwiger's Theorem

At a first glance, Minkowski numbers appear to be yet another characterization of some properties of a geometric object. What makes them particularly appealing though is a theorem due to Hadwiger (1957), cited in Mecke (2000), which states that any functional $\varphi(X)$ that depends on the object's form alone and that is additive, motion invariant, and continuous may be written as a linear combination of Minkowski numbers. Hence

$$\varphi(X) = \sum_{k=0}^{d} c_k M_k(X) \tag{6}$$

where c_k are real coefficients that depend on the property $\varphi(X)$ but are independent of the object X. Minkowski numbers thus form a complete basis of the space of all these functionals. This is the motivation for using Minkowski densities and density functions for quantifying complex patterns.

Calculation of Minkowski Numbers

Given the binary image of an object where each pixel is either 1 for the object or 0 for the background, the calculation of the Minkowski numbers is straightforward (Ohser and Mücklich, 2000). They can be obtained from a local evaluation of the pixel configuration within a 2×2 neighbourhood at each location within the image. There are $n = 2^4 = 16$ possible configurations q, each of them with a specific contribution to the different Minkowski numbers: (i) the number of pixel belonging to the object is related to M_0, (ii) the number of transitions $1 \leftrightarrow 0$ leads to M_1, and (iii) the number of vertices (pixels), edges and faces, N_v, N_e, and N_f, respectively, is related to $M_2 = 2\pi\chi$ by the classical Euler formula

$$\chi = N_v - N_e + N_f \tag{7}$$

In Figure 2, all 16 configurations q together with their specific contributions $I_k(q)$ are shown. The Minkowski densities may thus be calculated from the frequencies

$$f(q) = \frac{N(q)}{\sum_{q=0}^{15} N(q)} \tag{8}$$

of the different configurations within an image, where $N(q)$ is the number of 2×2 neighbourhoods with configuration q. The Minkowski densities may thus be calculated as

$$m_k = \omega_k \sum_{q=0}^{15} I_k(q) f(q); \quad k = 0, 1, 2 \tag{9}$$

where

$$\omega_0 = \frac{1}{\sum_q f(q)} \tag{10}$$

$$\omega_1 = \frac{\pi}{4} \frac{1}{[\lambda + \sqrt{2}\lambda] \sum_q f(q)} \tag{11}$$

$$\omega_2 = \frac{2\pi}{\lambda^2 \sum_q f(q)} \tag{12}$$

and λ is the side length of 1 pixel. We comment that these weights are correct only for the special case of square pixels and must be adapted for other shapes (Ohser and Mücklich, 2000). Similarly, the pattern to be analysed must be isotropic, without preferred directions, at least microscopically. However, they may be anisotropic macroscopically.

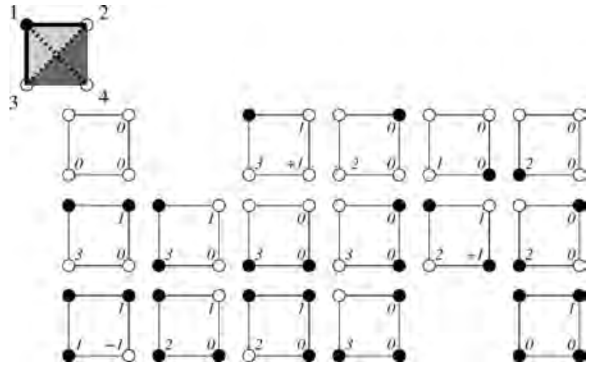

Figure 2 Complete set of the 16 possible pixel configurations in a 2×2 neighbourhood for a two-dimensional binary image. Pixels that belong to the object X are represented by a black circle. For each configuration, its contribution to M_0 (top right), M_1 (lower left), and M_2 (lower right) is given. The mode of evaluation is illustrated in the small figure at top left: For the contribution to M_0 the upper left pixel is considered. For the contribution to M_1 the transitions $1 \leftrightarrow 0$ are counted for the directions indicated by thick lines, including the two dashed ones. For M_2, the upper left vertex (pixel), the solid thick edges (provided they connect two occupied pixels), and the two grey shaded faces (provided they have three occupied vertices) are considered and evaluated according to (7).

Minkowski Density Functions

The $d + 1$ Minkowski densities characterize a particular binary representation of an object. A natural extension is to consider some transformation of the

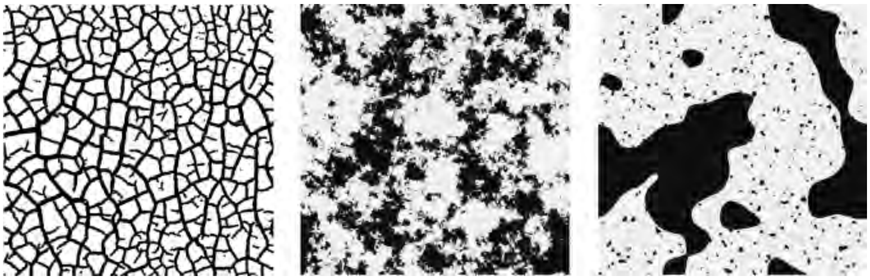

Figure 3 Exemplary 'pure' patterns—single-scale (left), fractal (middle), multiscale (right)—for which the Minkowski functions are shown in Figure 4.

original object or of its binary representation and to calculate Minkowski densities as functions of this transformation's parameter vector $\mathbf{p}$. This leads to the Minkowski density functions $m_k(\mathbf{p})$. In this work, we will use three particularly useful transformations:

1. Given a grey-scale image, binary representations are obtained for different values of threshold g_0 and m_k is calculated for them. The resulting functions $m_k(g_0)$ for instance facilitate choosing g_0 such that an optimally and objectively segmented pattern results. The generalization to colour images is straightforward.
2. To study the spatial variability of Minkowski numbers within a given pattern, m_k is calculated locally over a circular region of radius r to obtain $m_k(\mathbf{x}, r)$ for the intersection of the original pattern with a circle of radius r located at $\mathbf{x}$. This allows the identification of similar features within a given pattern.
3. To gain insight into the size distribution of features, the original pattern is opened with a circular element of radius r, i.e. all features of the pattern that are smaller than r are removed (Serra, 1982). This transformation is quite powerful, but may not be well-known. It is thus illustrated in the following with some artificial patterns before turning to the real application.

We choose three qualitatively different examples, (i) a single-scale pattern deduced from a cracked soil surface, (ii) a scale-free fractal pattern, and (iii) a multiscale pattern with a discrete hierarchy of scales (Figure 3). For each of these examples, we consider the black part as the pattern to be described. Opening it by radius r consists of two steps: First, it is eroded by radius r, i.e. the fraction that is within a distance r from the interface to the white part is chipped away. Some of the smaller pieces or narrow bridges between larger patches are thereby removed completely as illustrated in Figure 1. In the second step, the remaining black part is dilated, again with radius r, i.e. a 'skin' of thickness r is added. This two-step procedure effectively removes all features smaller than r and leaves the larger ones untouched. With this background, we look at the Minkowski density functions $m_k(r)$ for the three exemplary artificial patterns (Figure 4). Since we are not concerned with the real extent of the structures it is convenient to measure all distances in units of a pixel, which gives the resolution of the pattern. Notice that a 'pixel' usually refers to an area element while we will use the name for the side length of such a (quadratic) element.

First consider the single-scale pattern which essentially consists of a network of black lines that are of roughly equal thickness. Since there are many more closed loops (redundant connections) than isolated objects, the Euler number and thus m_2 is negative. The first opening step leaves the pattern practically unchanged because the surface is rather smooth. Hence, also the Minkowski numbers are practically constant. Increasing r further removes some of the bridges. Since these are roughly linear elements, the area density m_0 and the boundary density m_1 decrease by comparable factors. Removing bridges destroys loops and creates isolated patches. Hence m_2 increases and eventually becomes positive thereby indicating that isolated patches outnumber the redundant connections. We finally notice that the thickest structure in the original pattern has a diameter of 8 pixel: opening with $r = 4$ pixel removes the entire pattern since then $m_0 = 0$.

The second example, the fractal pattern, is of a completely different character. As m_2 reveals and as is quickly confirmed by looking at Figure 3, tiny isolated patches greatly outnumber loops. What is less obvious, however, is that removing these small structures by an opening with $r = 1$ pixel creates a pattern where loops outnumber patches. This swings back once more for $r > 2$ pixel. Concerning the size

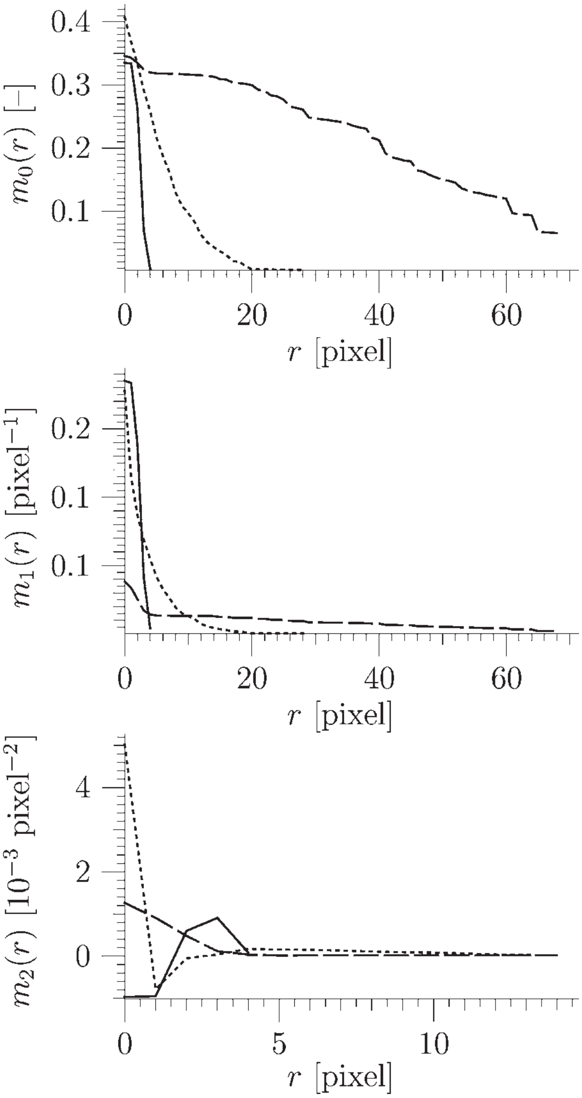

Figure 4 Minkowski density functions for the single-scale (solid), fractal (dotted), and multiscale (dashed) pattern shown in Figure 3. Notice the different scale of r for m_2 as compared to m_0 and m_1.

distribution, we conclude from the continuous decline of m_0 and m_1 with increasing r that the distribution is smooth and that the original pattern has no natural length scale beyond the trivial ones that are given by the size of a pixel and by the extent of the entire region. Plotting $\log(m_0)$ and $\log(m_1)$ versus $\log(r)$ would show if the pattern is indeed a simple fractal and would yield the respective dimensions.

Finally, the third example is revealed as a multi-scale pattern by both m_0 and m_1, and m_2 shows that it essentially consists of the superposition of patches. The clearest evidence of the multiscale architecture stems from $m_1(r)$ whose slope changes abruptly at $r = 4$ pixel. The minute change of m_0 for $r < 4$ pixel shows that the areal fraction of these small-scale structures is also small. Based on the information so far, one cannot decide if they result from surface roughness or if they are small isolated patches. However, the rapid decrease of m_2 reveals that the latter is the case. Removing surface roughness would not affect the value of m_2 since no objects are created or removed.

APPLICATION

Permafrost patterns are typically not as uniform as the examples considered above and the base information is in general not in binary form. Nevertheless, Minkowski numbers and functions are a powerful tool for the quantitative analysis and interpretation of such patterns. This is demonstrated in the following for the surface patterns at two permafrost sites that are only a short distance apart. In particular, we focus on the pattern of vegetated areas.

Material

We use aerial images taken on Howe Island (N70°18′, W147°59′), located off the Alaskan Arctic coast, northeast of the Prudhoe Bay oil fields (Figure 5). The surface is loess overlaid by stabilized alluvium. Bare soil, partly encrusted with salt or cryptograms, covers 80–90% of the area. Dominant patterned ground forms are high- or flat-centred ice-wedge polygons tens of metres in size and non-sorted circles, also called mud boils or frost boils with diameters of 1–2 m. The non-sorted circles are either continuous patches of bare soil or are broken into smaller sized polygons with diameters of 0.1–0.4 m. Vegetation, mainly discontinuous prostrate shrubs, inhabits the borders of the bare ground circles and ice-wedge polygonal troughs where water content is higher. The organic layer is thin, typically less than 3 cm.

Aerial images were taken with a digital camera (Olympus C2020) suspended from a kite (Boike and Yoshikawa, 2003). The camera contains an interlaced RGB CCD with 1600 × 1200 square photo receptors. Images were obtained at the camera's largest focal length, 19.5 mm corresponding to 105 mm for a 35 mm camera, and stored at highest resolution. The ground resolution of the images as calculated from a few reference marks are approximately 37 mm per pixel at site H1 and 29 mm per pixel at site H2. Again, we are not concerned with the real extent of the structures and will measure all distances in units of a pixel.

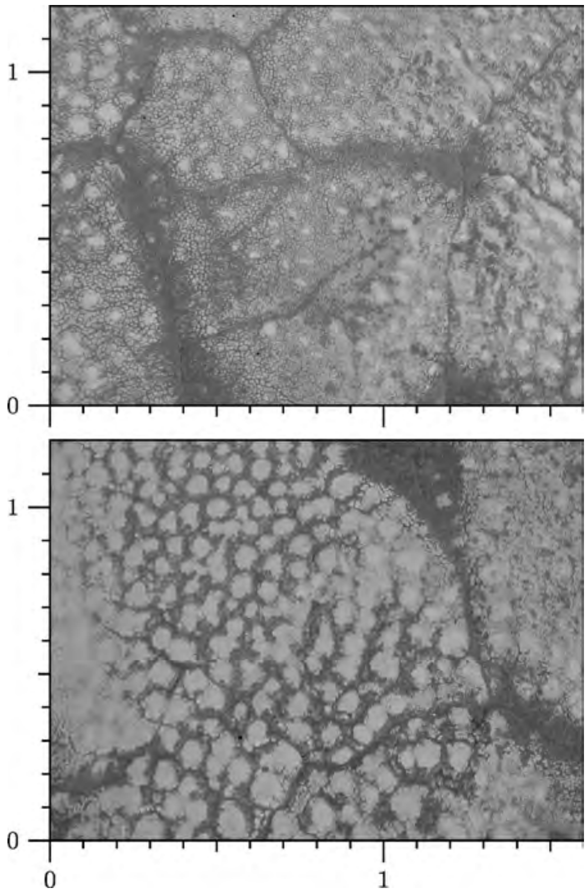

Figure 5 Original aerial images from sites H1 (top) and H2 (bottom). The discontinuous vegetation cover appears darker in contrast to the lighter bare ground, distinguishing the patterned ground features. At site H1, the polygonal ice-wedge network, non-sorted circles and small non-sorted polygons can be distinguished. Site H2 is largely dominated by non-sorted circles, each surrounded by a vegetated border. Distance units at the axes are kpixel with a resolution of some 37 m/kpixel at H1 and 29 m/kpixel at H2.

Prior to analysis, the aerial photographs were processed through the following steps: (i) Transformation of RGB colour image into an eight-bit grey scale representation (256 levels of grey) by averaging the three colour channels. (ii) Stretching contrast of the image such that the darkest 1% of the pixels turn black and the lightest 1% turn white with linear interpolation in between. (iii) The last step, inverting the image, was done only to facilitate the perception of the pattern of interest.

We comment that, for precise quantification, a few more preliminary steps would be required. These include transforming the original image into an orthonormal representation and correcting possible nonuniform illumination. Both steps require a number of reference marks on the ground that are not available for the images used here. Notice that while this renders the numbers obtained from the subsequent analysis less useful for a detailed quantitative analysis, it does not compromise the qualitative comparison of different patterns.

The most crucial step with respect to applications is the segmentation of the image, i.e. the transformation of the grey-scale image into a binary representation since this determines what features will eventually be analysed. In general this will be a rather complicated step that requires input from different colour channels of the image and possibly some ancillary information like surface topography. Since our focus is on pattern analysis, however, we will employ the most simple threshold method. We thus choose an appropriate threshold g_0 for the grey value g and assign the value 0 (white) to pixels for which $g < g_0$ (vegetated surface) and the value 1 (black) to all others (bare surface). For site H1, results of preliminary image processing and segmentation with some distinguished values of g_0 are shown in Figure 6. In the following, we will refer to the black part of the pattern, which corresponds to the bare soil, as the 'black phase'. Consequently, the vegetated soil surface is represented by the 'white phase'.

Dependence of Minkowski Densities on Segmentation Threshold

We consider the black phase of binary representations of sites H1 and H2 to study the dependence $\bar{m}_k$ on the segmentation threshold g_0 (Figure 7). The notation $\bar{m}_k$ is chosen to distinguish the Minkowski densities of the entire pattern from those of subregions which will be introduced in subsequent sections.

As expected, $\bar{m}_0$, which equals the area fraction of the black phase, increases monotonically with g_0. It actually is the probability distribution function of the grey values. Apparently, the area fraction increases more rapidly for smaller values of g_0 at site H2 than at H1. This results from the large patches of bare soil that also stand out in Figure 5.

The number $\bar{m}_1$ corresponds to the length density of the interface between the black and white phases. For the type of regular structure considered here, $\bar{m}_1$ may be expected to be small for extreme values of g_0 since the corresponding patterns consist mainly of small black or white patches. Provided the character of the interface, in particular its variation, does not depend on g_0 there will be a monotonic relation between the area of an object and its interface length. As long as the patches remain isolated, we thus expect

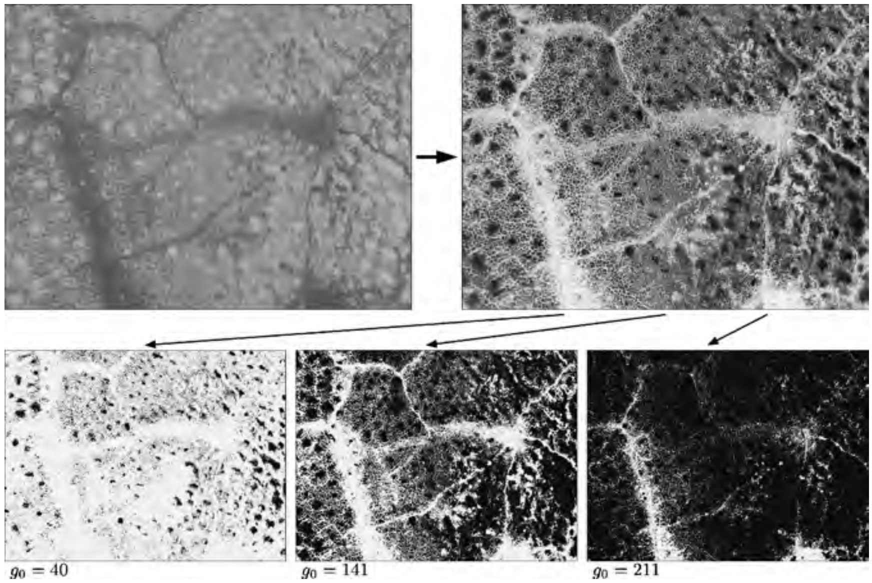

Figure 6 Preliminary image processing consists of transformation from RGB to grey scale (upper left), contrast stretching, and inversion (upper right). Segmentation with threshold g_0 then leads to a binary representation of the pattern (bottom row). The value of g_0 is chosen such that m_2 is maximal ($g_0 = 49$), zero ($g_0 = 141$), and minimal ($g_0 = 211$), respectively.

a monotonic increase of $\bar{m}_1$ as g_0 departs from the extreme value. This general behaviour is realized at both sites. For intermediate values of g_0, the shape of $\bar{m}_1(g_0)$ reflects the respective gains and losses of interfacial area as new objects occur and coalesce, respectively. The two sites show marked differences in that the two overlapping peaks for site H2 indicate the existence of two separate classes of objects with different brightnesses whereas the single-peaked shape for site H1 hints at a more uniform distribution of brightnesses.

We finally consider $\bar{m}_2$ which is proportional to the Euler number of the black phase. We recall that $\bar{m}_2$ is a topological quantity, in contrase to $\bar{m}_0$ and $\bar{m}_1$ which are metric quantities. In two dimensions, it gives the difference between the numbers of isolated objects and redundant connections, divided by the total area. As already noted in the previous paragraph, for extreme values of g_0 we expect the pattern to consist predominately of isolated patches (see Figure 6). These will be black patches for small values, representing isolated objects, and white patches for large values, corresponding to holes, hence to redundant connections. Thus, $\bar{m}_2$ is expected to be positive for small values of g_0 and negative for large ones. With g_0 departing from its extremes, the number of objects will initially increase, leading to a corresponding increase of the magnitude of $\bar{m}_2$. Eventually, with g_0 departing further, more isolated black and white objects will merge than there are created and the magnitude of $\bar{m}_2$ will decrease. We thus expect to find at least two extrema in $\bar{m}_2(g_0)$, one positive towards small values of g_0 and one negative towards large values. For both sites, this general shape is clearly discernible in the lower graph of Figure 7. For intermediate values of g_0, we may expect quite some variability for the shape of $\bar{m}_2(g_0)$ between different sites, as is already the case for the two sites considered here. Looking at H2, we find from $\bar{m}_0$ that the area fraction with grey values in the interval (100,150) is about 0.15 and that also the length of the interface as shown by $\bar{m}_1$ changes significantly in this interval. However, $\bar{m}_2$ is approximately constant in this interval which means that if the number of objects changes at all, this change is balanced by the number of redundant connections. This indicates that the topology of the black phase does not change significantly in this interval. The situation is quite different at site H1, where we find a continuous change of the metric and of the topological quantities.

As a final remark, we notice that the functions $\bar{m}_k(g_0)$ are approximately orthogonal, i.e.

$$\sum_{i=0}^{255} \left[\bar{m}_j(i) - \langle \bar{m}_j \rangle\right]\left[\bar{m}_k(i) - \langle \bar{m}_k \rangle\right] \approx 0, \quad j \neq k \quad (13)$$

where $\langle \bar{m}_j \rangle := 256^{-1} \sum_{i=0}^{255} \bar{m}_j(i)$. This means that the three functions $\bar{m}_k(g_0)$ contain approximately

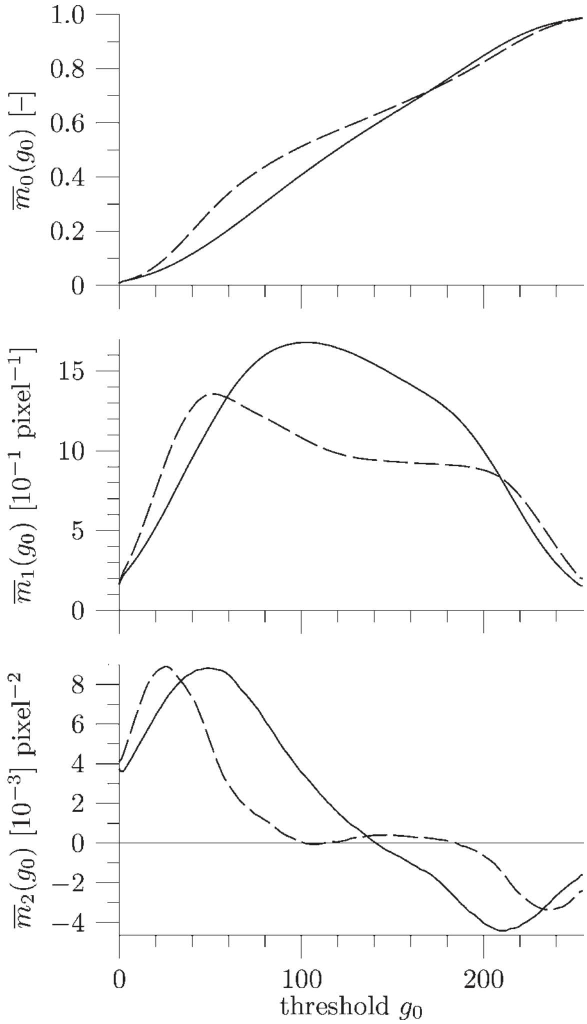

Figure 7 Global Minkowski density functions $\bar{m}_k(g_0)$ for the black phase of binary representations of H1 (solid) and H2 (dashed).

independent information on the pattern as a whole. Notice that this is a different statement from Hadwiger's theorem which only refers to the binary representation of the pattern for a particular value of g_0. Clearly, these functions cannot reveal detailed structures of the image but rather are lowest order descriptions. Their use would be analogous to that of statistical moments for characterizing probability density functions. It appears to be worthwhile to explore to what extent different patterns occurring in nature can be categorized simply by the shape of the corresponding Minkowski density functions $\bar{m}_k(g_0)$. Obviously, a quantitative exploration of this requires carefully normalized images which in turn demands a set of reference marks on the ground. However, if these are not available, as will often be the case, qualitative comparison is possible even with the type of rough normalization described in Material. We will not follow this line here, however, and proceed to analyse the spatial structure in more detail.

Spatial Variability of Minkowski Densities

Natural patterns often contain elements on different scales as is also the case for the two permafrost sites considered here. It is thus useful to calculate the Minkowski densities not only for the entire field of view but also for subregions. The first question arising concerns the size of these subregions. As a pragmatic approach, we employ the concept of the representative elementary volume (REV), choose circular subregions with radius r, calculate m_k at different locations as a function of r, and choose r such that the circle encompasses small-scale variations but is not yet affected by large-scale variations. Figure 8 shows $m_k(r)$ for a few typical locations at H1 with $g_0 = 141$. For small values of r, less than 30 say, m_k strongly depends on the immediate neighbourhood and thus fluctuates strongly with r. However, with increasing values of r, $m_k(r)$ often approaches a rather constant value that is representative for the small-scale patterns. In some instances, m_k becomes stable only for very large values of r. These typically correspond to locations that are near the boundary between some large-scale features. From Figure 8, we choose $r = 50$ as a reasonable radius for an REV.

With an REV in hand, we explore the spatial variability of the Minkowski densities by assigning to each location **x** the value of m_k in the REV centred at **x**. Figure 9 shows the resulting density functions for the black phase of H1 with segmentation threshold $g_0 = 141$.

We first notice that the large-scale features of the pattern are visible in all three Minkowski densities even though the details are characteristically different. Easiest to interpret is m_0, which in two dimensions equals the areal density of the phase considered. It clearly identifies regions of extended vegetated patches (low values of m_0), of extended bare patches (high values of m_0), and of the rather wide transition regions between. Obviously, we lack the spatial resolution of the original image and thus cannot say anything about the structures of the transition regions which could be larger isolated lumps as well as finely interweaved phases. This information is to some extent contained in the Minkowski densities m_1 and m_2, however.

In regions with extreme values of m_0 either the black or the white phase dominates strongly.

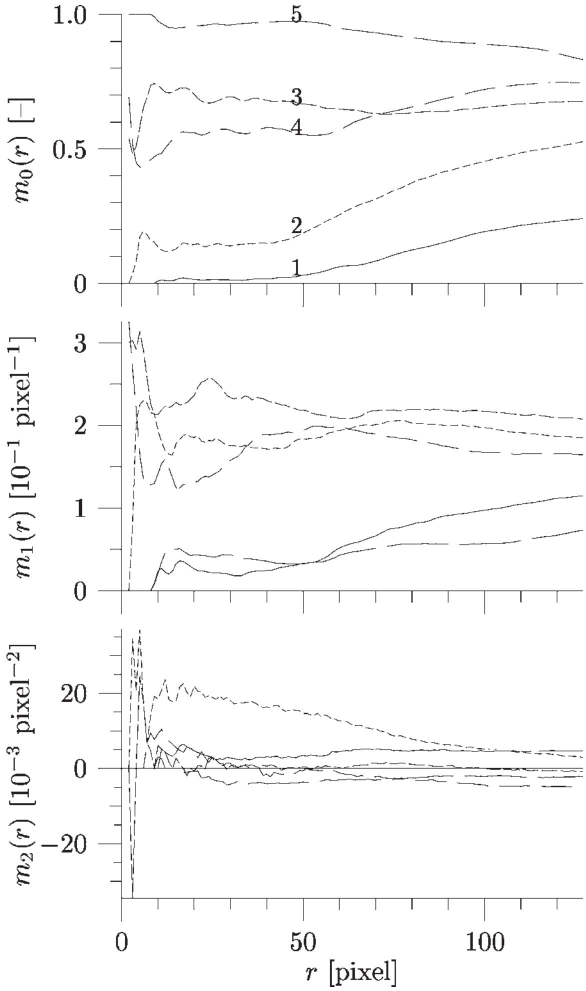

Figure 8 Typical examples for the dependence of Minkowski densities m_k *on radius* r of circular subregions (black phase of H1 for $g_0 = 141$). The numbers that identify the curves in the top graph correspond to the locations given in Figure 9.

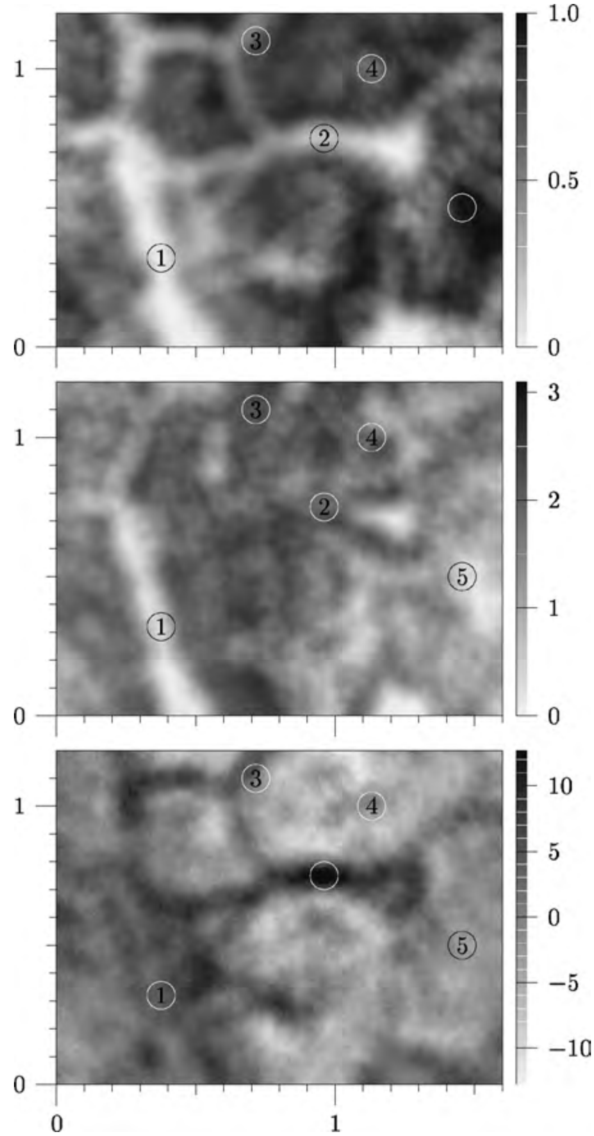

Figure 9 Spatial variability of Minkowski densities m_0 (top), m_1 [10^{-1} pixel^{-1}] (middle), and m_2 [10^{-3} pixel^{-2}] (bottom) for the black phase of H1 with threshold $g = 141$. The corresponding pattern is shown in the upper left of Figure 10. Numbers are calculated for circular areas with radius $r = 50$ pixel and plotted with a resolution of 10 pixel. Axes are labelled in kpixel. Numbered circles identify locations with radius $r = 50$ pixel used for Figure 8.

Correspondingly, the density of interfaces between them is small. Examples are the regions around $\mathbf{x} = (1.2, 0.7)$ and $\mathbf{x} = (1.5, 0.45)$ where m_0 is smaller than 0.1 and larger than 0.9, respectively. In both regions, we find values of m_1 that are more than an order of magnitude smaller than the largest values at this site. Transition regions on the other hand, with values of m_0 around 0.5, may contain high or low densities of interfaces, depending on the arrangement of the phases. Examples for regions with comparable values of m_0 but quite different values of m_1 are around $\mathbf{x} = (0.7, 0.35)$ and $\mathbf{x} = (1.3, 0.5)$.

Further information about small-scale structures, namely about their connectivity, is contained in m_2 which in two dimensions is proportional to the difference between the number of isolated objects and the number of redundant connections of the black phase. Regions with comparable values of m_0 and m_1 may thus be discriminated with respect to m_2. An example is provided by the surroundings of $\mathbf{x} = (0.45, 0.65)$

and $\mathbf{x} = (1.1, 1.0)$. We further find that the black phase, which corresponds to the bare soil regions, consists of predominantly isolated objects near the boundaries of the large-scale features while in their interior the black phase is connected.

Of course, visual inspection also provides the information just outlined. The advantage of using Minkowski densities is that we can easily quantify such subjective impression and that inspection can be performed automatically, thereby facilitating the precise monitoring of large areas.

Comparing Sites

We compare the binary representations of H1 with $g_0 = 141$ and of H2 with $g_0 = 102$, respectively, which are shown in Figure 10. These values are chosen such that $\bar{m}_2 \approx 0$ for the global pattern at the respective site (see Figure 7). The density functions $m_0(\mathbf{x}), \ldots, m_2(\mathbf{x})$ are shown in the top rows of Figures 11–13 with the same resolution as used for Figure 9. As already mentioned, m_0 discriminates between solid patches and open transitional regions. Obviously, the forms of the transitional regions differ considerably between the two sites, with an apparent multiscale organization at H1 and dominating single scale shapes at H2. While this is reflected in considerably larger interface densities at H1 as compared to H2 (see also Figure 14 with $r = 0$) the difference is most pronounced in the spatial variation of m_2. At H1, the connectivity varies greatly in space. Regions with a highly connected black

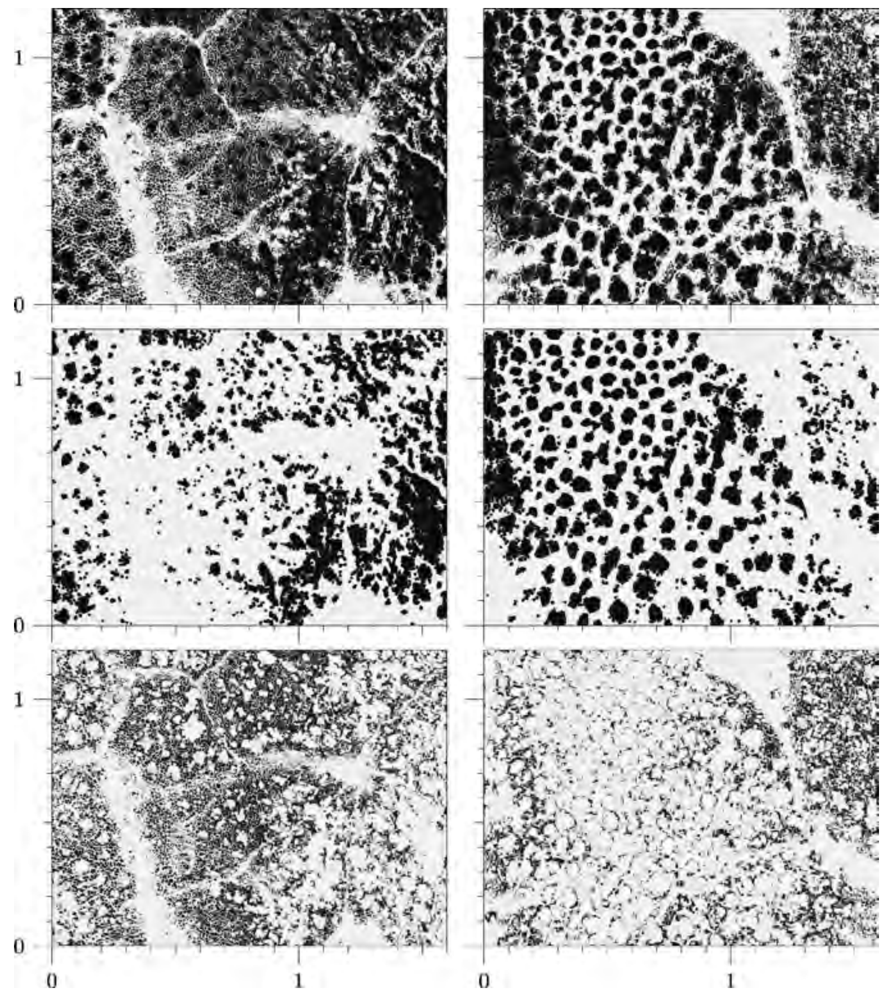

Figure 10 Binary representations of H1 with $g_0 = 141$ (left column) and of H2 with $g_0 = 102$ (right column) before (top row) and after (middle row) opening with a circular element of radius 5 pixel. The bottom row shows the difference between the original and the opened pattern, i.e. those parts of the patterns are smaller than a circle with $r = 5$ pixel. Axes are again in kpixel.

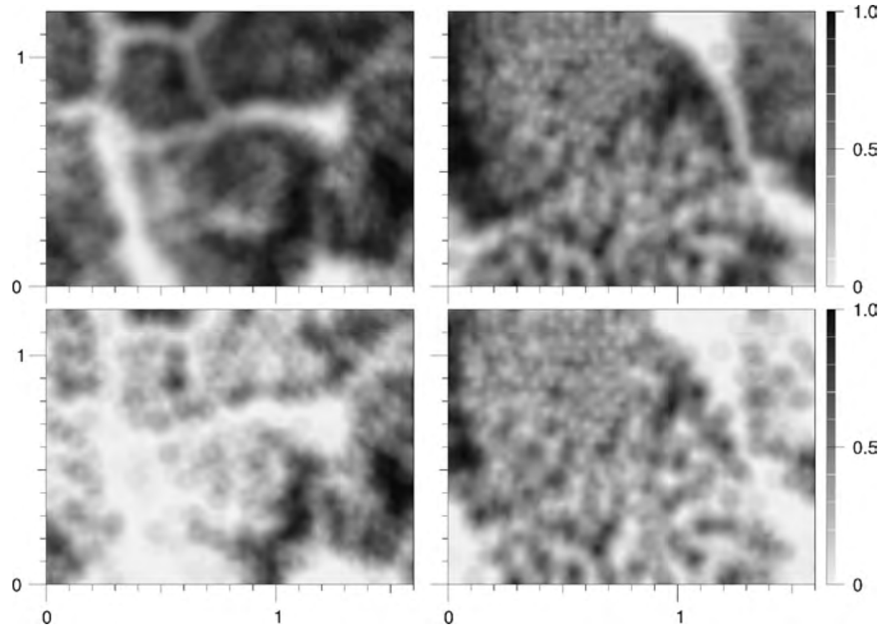

Figure 11 Minkowski density m_0—the area fraction of black phase—for the original patterns shown in the top row of Figure 10 (top row) and for the patterns opened with $r = 5$ pixel shown in the middle row of Figure 10 (bottom row). The left column is for site H1, the right one for H2. Grey-scale is dimensionless.

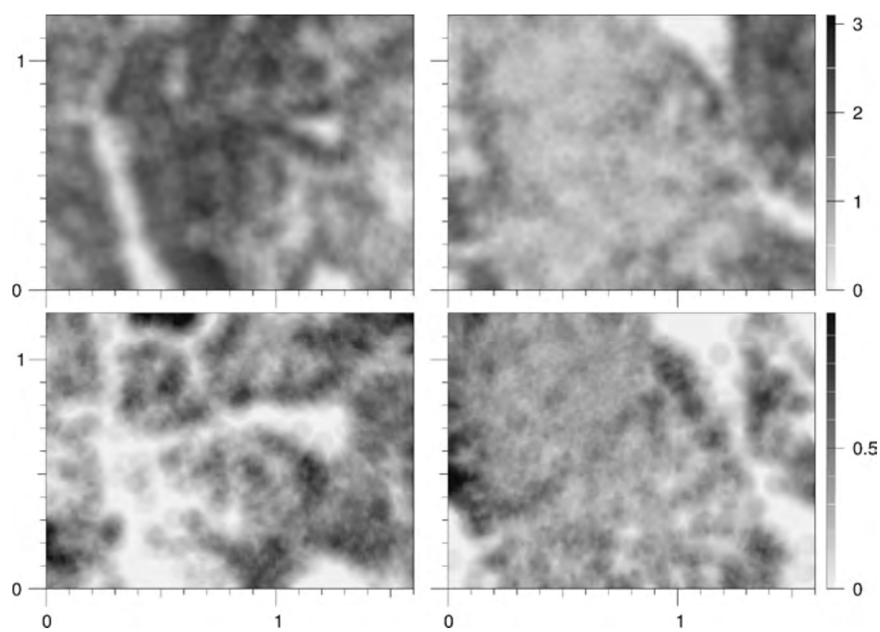

Figure 12 As Figure 11 but for Minkowski density m_1, the surface density. Notice the different grey scales. Their units are $10^{-1}\,\text{pixel}^{-1}$.

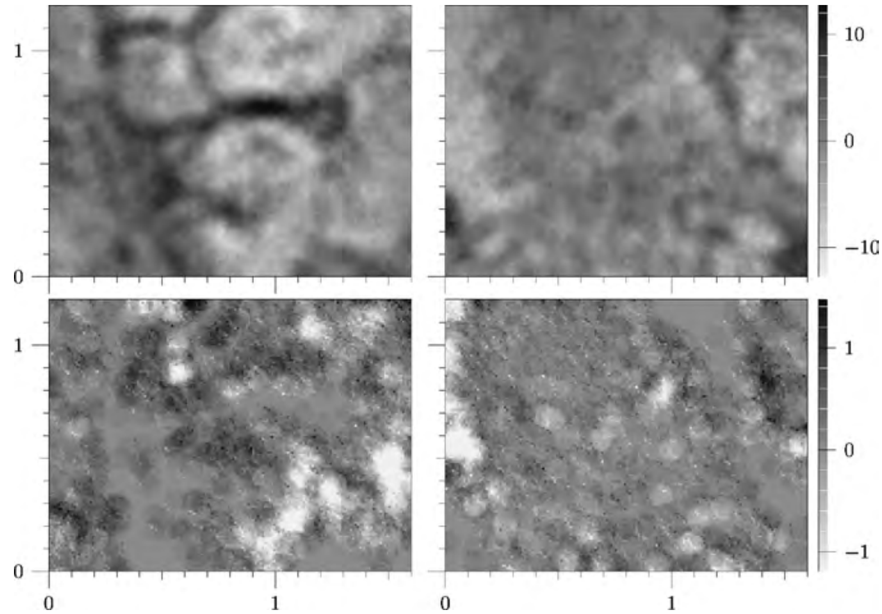

Figure 13 As Figure 11 but for Minkowski density m_2, the Euler number density. Notice the different grey scales. Their units are 10^{-3} pixel^{-2}.

phase, $m_2 > 10^{-2}$ pixel^{-2}, are adjacent to regions where the black phase essentially consists of isolated objects, $m_2 < -10^{-2}$ pixel^{-2}. At H2 in contrast, m_2 is rather uniform over most of the field with values between $\pm 10^{-3}$ pixel^{-2}.

As pointed out above, a more detailed analysis is possible by looking at opened patterns for which elements that are smaller than a circle with some radius r are removed. Opening has three effects on a pattern: (i) interfaces are smoothed which reduces their length, (ii) narrow bridges between larger patches are removed which tends to increase the number of isolated objects and at the same time to reduce the number of redundant connections, and (iii) small objects are removed entirely. Clearly, the impact of opening depends strongly on the organization of a pattern, as is illustrated by the bottom row of Figure 10 where those features are depicted that disappear upon opening with $r = 5$ pixel. Opening the pattern removes 55% of the black phase at H1, $\bar{m}_0$ decreases from 0.60 to 0.28, but only 36% at H2 (Table 1). Corresponding to the decrease in $\bar{m}_0$ and the interfacial smoothing, we also find a strong decrease of the interfacial length density $\bar{m}_1$ which decreases to 23% of its original value at H1 and 32% at H2. We remark that in contrast to $\bar{m}_0$, $\bar{m}_1$ need not decrease with opening, although it usually will with the type of patterns considered here. While $\bar{m}_0$ and $\bar{m}_1$ are typically found to be monotonically decreasing functions of the opening radius, $\bar{m}_2$ will in general be of a rather complicated form. The reason for this is that opening removes small isolated objects, thereby reducing $\bar{m}_2$, but also removes narrow bridges which creates new objects and reduces connections, causing $\bar{m}_2$ to increase.

More important than the different average changes of $\bar{m}_0$ at the two sites, however is that the opening at H1 removes an entire feature of the pattern, namely the small polygonal bare patches along the boundary between the largest structures (see bottom row of Figure 10). In contrast, opening at H2 leads to rather minor modifications, mostly to interface smoothing. This difference is also manifest in the spatial structure of the Minkowski densities (bottom rows of Figures 11–13). At H1, the original large regions of rather compact black phase have almost disappeared with only small patches remaining (Figure 11), the regions with negligible interfacial length density are greatly enlarged (Figure 12), and the connectivity patterns change completely with some highly connected regions transformed into ones with predominantly isolated objects, for instance near $\mathbf{x} = (0.8, 1.0)$ (Figure 13). In contrast, the changes at H2 are rather moderate with the overall structure hardly affected over most of the region. An exception to this are small regions, for instance around $\mathbf{x} = (0.1, 0.6)$ and $\mathbf{x} = (1.5, 0.8)$, which are structurally more similar to H1. This comparison demonstrates the power of Minkowski densities to

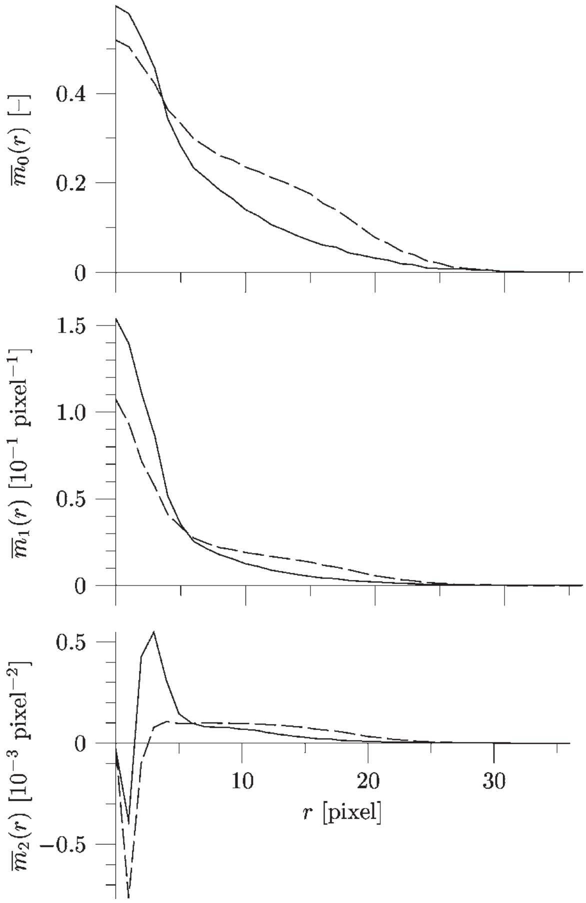

Figure 14 Minkowski densities $\bar{m}_k$ as functions of the opening radius r at sites H1 (solid) and H2 (dashed).

identify and quantify multiscale organizations of patterns as they are encountered at H1 but not at H2.

We comment that the analysis just presented could be sharpened further by discriminating between different sub-patterns and by then restricting the calculation of $m_k(\mathrm{x})$ to similar sub-patterns. Figure 10 shows for instance that the top right corner at H2 is structurally more similar to the pattern found predominantly at H1 than to the rest of the pattern at H2. Such a discrimination could be readily automated since the patterns can be distinguished based on their Minkowski densities.

Table 1 Global values of Minkowski densities $\bar{m}_k$ before and after opening by a circle with radius of 5 pixel.

k	H1	H2	H1$^{\text{open}}$	H2$^{\text{open}}$	Units
0	0.60	0.52	0.28	0.33	1
1	1.54	1.07	0.35	0.34	10^{-1} pixel^{-1}
2	−0.038	0.032	0.144	0.096	10^{-3} pixel^{-2}

Minkowski Density Functions

We consider the global Minkowski densities $\bar{m}_k$ as functions of the opening radius r, again for binary representations of H1 with $g_0 = 141$ and of H2 with $g_0 = 102$ (Figure 14). The multiscale organization of the pattern at H1 postulated in the previous section becomes further manifest in that both $\bar{m}_0$ and $\bar{m}_1$ decrease rather rapidly for $r < 6$ pixel and tail off for larger values of r. In comparison, the decrease at H2 is more gradual. An even stronger discrimination between the two sites is apparent in $\bar{m}_2$. The initial opening step makes $\bar{m}_2$ more negative at both sites, although the effect is much stronger at H2 than at H1. Inspection of the images (not shown) reveals that the strong decrease of $\bar{m}_2$ results from a large number of small objects that get removed even though some redundant connections also disappear. At H2, the following opening steps let $\bar{m}_2$ jump to slightly positive values where it remains practically constant for $3 \leq r < 12$ and decreases slowly to 0 afterwards. This indicates that for a rather extended range of sizes, the topology of the pattern remains constant. At H1, in contrast, opening beyond the first step leads to a very strong increase of $\bar{m}_2$ which is caused by the creation of isolated objects by eroding away narrow necks with widths between 2 and 4 pixel. These newly formed isolated objects are rather small, however, and disappear rapidly upon further opening. With $r > 5$ pixel, $\bar{m}_2$ continues to decrease, but at a more moderate rate.

As an aside, we comment that log-log plots of $\bar{m}_0$ and $\bar{m}_1$ at the two sites show that the interfacial length density at H2 may follow a power law distribution, but that the other quantities are of a more complicated form. The underlying patterns thus cannot be described as simple fractals.

SUMMARY AND CONCLUSIONS

We have introduced Minkowski densities and density functions as tools for quantifying patterns and demonstrated them by analysing three artificial patterns. We then applied them to aerial images obtained from patterned ground at two neighbouring permafrost sites. Although these tools cannot rival our visual perception in discriminating and possibly also in categorizing natural patterns, they do have two significant advantages:

1. They can be performed automatically and thus facilitate the analysis of very large data sets as

for instance produced by high-resolution satellite imagery. Automated analysis is typically most efficient with some initial manual adjustment of parameter ranges, most importantly for thresholds and averaging areas in case of spatially varying patterns. However, even those steps can be automated with more sophisticated algorithms that implement and combine the analyses that led to Figures 7 and 8. Exemplary visual inspection of the results will remain mandatory as with all automated procedures.
2. They are quantitative, hence allow us to monitor transitions in space and changes in time in an objective manner that does not depend on the interpreter's experience and form. This also facilitates comparisons of patterns from different sites.

We should comment in closing that the methods introduced here reduce an arbitrary pattern to a few numbers or at most to a few functions. Clearly, a huge fraction of the information contained in the pattern is thereby lost and it will, in particular, not be possible to recreate the pattern from the reduced information. Such data reductions are well known from statistical analyses where rich data sets are reduced to their first few moments, e.g. mean and variance, and the corresponding functions, e.g. the autocovariance. The power of such reductions is their focusing on just a few aspects and in eliminating all the others. They are only useful to the extent that the focused aspects are of interest. However, since areal fractions, interface densities, connectivities, and distances to interfaces are relevant for many functional aspects of a permafrost environment, Minkowski numbers and functions are proposed as a useful tool for quantifying the observed patterns.

Implementations of the tools used in this work are contained in the public domain package QuantIm which may be obtained from www.iup.uni-heidelberg.de/institut/forschung/groups/ts/tools.

ACKNOWLEDGEMENTS

Thanks to D. A. (Skip) Walker, Vladimir Romanvosky, Chien-Lu Ping, and Martha (Tako) Raynolds of the research project 'Biocomplexity on frost boil ecosystems' who supported field work and provided valuable discussion on the site. JB gratefully acknowledges financial support by the Deutsche Akademie der Naturforscher Leopoldina (BMBF-LPD 9901/8-11). An anonymous reviewer helped us greatly to improve the accessibility of the somewhat abstract concepts.

REFERENCE

Bacry E, Delour J, Muzy JF. 2001. Multifractal random walk. *Physics Review E* **64**(026103): 1–4.

Boike J, Yoshikawa K. 2003. Mapping of periglacial geomorphology using kite/balloon aerial photography. *Permafrost and Periglacial Processes* **14**(1): 81–85. DOI: 10.1002/ppp.437

Francou B, Méhauté NL, Jomelli V. 2001. Factors controlling spacing distances of sorted stripes in a low-latitude, alpine environment (Cordillera Real, 16°S, Bolivia). *Permafrost and Periglacial Processes* **12**: 367–377. DOI: 10.1002/ppp.398

Hadwiger H. 1957. *Vorlesungen über Inhalt, Oberfläche und Isoperimetre*. Springer-Verlag: Heidelberg.

Hallet B. 1990. Self-organization in freezing soils: from microscopic ice lenses to patterned ground. *Canadian Journal of Physics* **68**: 842–852.

Journel AG, Huijbregts C. 1978. *Mining Geostatistics*. Academic Press: San Diego.

Kessler MA, Murray AB, Werner BT, Hallet B. 2001. A model for sorted circles as self-organized patterns. *Journal of Geophysical Research* **106**(B7): 13287–13306.

Mandelbrot B. 1977. *The Fractal Geometry of Nature*. Freeman: New York.

Mecke KR. 2000. Additivity, convexity, and beyond: applications of Minkowski functionals in statistical physics. In *Statistical Physics and Spatial Statistics. The Art of Analyzing and Modeling Spatial Structures and Pattern Formation*, Mecke KR, Stoyan D (eds). Springer Verlag: Berlin; Lecture Notes in Physics 554, 111–184.

Ohser J, Müucklich. 2000. *Statistical Analysis of Microstructures in Materials Science*. John Wiley & Sons: New York.

Serra J. 1982. *Image Analysis and Mathematical Morphology.* Academic Press: London.

van Kampen NG. 1981. *Stochastic Processes in Physics and Chemistry.* North-Holland: Amsterdam.